TEKTONIKA

Local Strain Reorientation Explains Deformation of Rift-oblique Tectonic Lineaments Along the Main Ethiopian Rift

Frank Zwaan [*1,2,3], **Ameha A. Muluneh** [1,4], **Jun Liu** [1,5], **Ehsan Kosari** [1], **Matthias Rosenau** [1], **Giacomo Corti** [6], **Federico Sani** [7]

[1]GFZ Helmholtz Centre for Geosciences, Telegrafenberg, 14473 Potsdam, Germany | [2]University of Fribourg, Department of Geosciences, Chemin du Musée 6, 1700 Fribourg, Switzerland | [3]University of Lausanne, Institute of Earth Sciences, Building Géopolis, UNIL-Mouline, 1015 Lausanne, Switzerland | [4]MARUM, University of Bremen, Leobener Staße 8, 28359 Bremen, Germany | [5]Department of Earth Sciences, Freie Universität Berlin, Malteserstraße 74-100 / Building A, 12249 Berlin, Germany | [6]CNR-IGG, Consiglio Nazionale delle Ricerche, Istituto di Geoscienze e Georisorse, Via G. La Pira 4, 50121 Firenze, Italy | [7]Università di Firenze, Dipartimento di Scienze della Terra, Via G. La Pira 4, 50121 Firenze, Italy

Abstract The interaction between the NE-SW striking Main Ethiopian Rift (MER) and the E-W oriented Yerer-Tullu Wellel Volcano-tectonic lineament (YTVL) represents one of the least understood tectonic problems in the East African Rift System. Despite the numerous studies that have been conducted in the region, the following questions still remain to be answered: did the MER and YTVL evolve simultaneously? Was there a change in plate motion direction to allow a diachronous evolution of the rift and the lineament? How does the E-W oriented YTVL remain active under ca. E-W oriented regional extension? Previous studies propose a two-phase tectonic evolution, involving a change in the direction of plate motion at around 6 *Ma* causing deformation to focus in the MER. However, this interpretation contradicts plate-tectonic reconstruction data suggesting a constant plate divergence direction since ca. 16 *Ma*. We use analogue models to study how deformation may occur along the YTVL. We find that the activation of lineaments oriented (near-)parallel to the plate divergence direction is in fact possible, if (1) the lineament sufficiently reduces the strength of the crust and (2) the main rift trend is sufficiently oblique to the overall plate divergence direction. We interpret this to be the result of a local reorientation of the regional extensional strain caused by the obliquity of the main rift, which allows for deformation along the otherwise unfavourably oriented lineament. As such, no multiphase scenario is required to explain the development of the YTVL, and a single-phase scenario that is in line with plate tectonic reconstructions can be adopted instead. Moreover, our model results suggest that other lineaments associated with the MER could also be active in the current tectonic regime. These insights may be of relevance to the interpretation of deformation along similar oblique structures associated with the MER, and with other past and present rift systems as well.

Executive Editor:
Janine Kavanagh
Associate Editor:
Guillaume Duclaux
Technical Editor:
Mohamed Gouiza

Reviewers:
L. Le Pourhiet
A. Samsu

Submitted:
15 July 2024
Accepted:
9 April 2025
Published:
22 August 2025

1 Introduction

The Main Ethiopian Rift (MER) forms the northern section of the East African Rift System (EARS) and connects the Afar depression in the north, where the EARS links with the Red Sea and Gulf of Aden Rifts, to the Turkana depression in the south (Figure 1 *Corti*, 2009). The MER is a narrow rift valley that accommodates the active extensional deformation between the diverging Nubia and Somalia Plates (e.g., *Michon et al.*, 2022). Nubia-Somalia divergence involves rotational plate motion, and as such, divergence rates along the EARS as a whole follow a southwardly decreasing trend, with implications for overall rift system development (e.g., *Zwaan and Schreurs*, 2020, 2023) (Figure 1a). However, at a more local scale, such as along the MER, this gradient is of no particular importance (*Zwaan and Schreurs*, 2020). Here, divergence currently occurs in a roughly E-W direction at rates of ∼4-6 *mm/yr* (*Saria et al.*, 2014; *Stamps et al.*, 2021, e.g.,), and plate kinematic models suggest this motion has been constant (in terms of plate divergence direction) over the last 16-17 *Myr* (*DeMets and Merkouriev*, 2021) (Figure 1).

The MER is generally considered to consist of three different sectors (Northern MER; Central MER and Southern MER; Figure 1), which differ in terms of orientation, fault pattern, crustal/lithospheric characteristics, age of onset of rifting and volcanism (e.g., *Corti*, 2009). The fault pattern in the different rift segments is dominated by large boundary faults separating the rift floor from the surrounding plateaus:

*✉ frank.zwaan@gfz.de | frank.zwaan@unil.ch

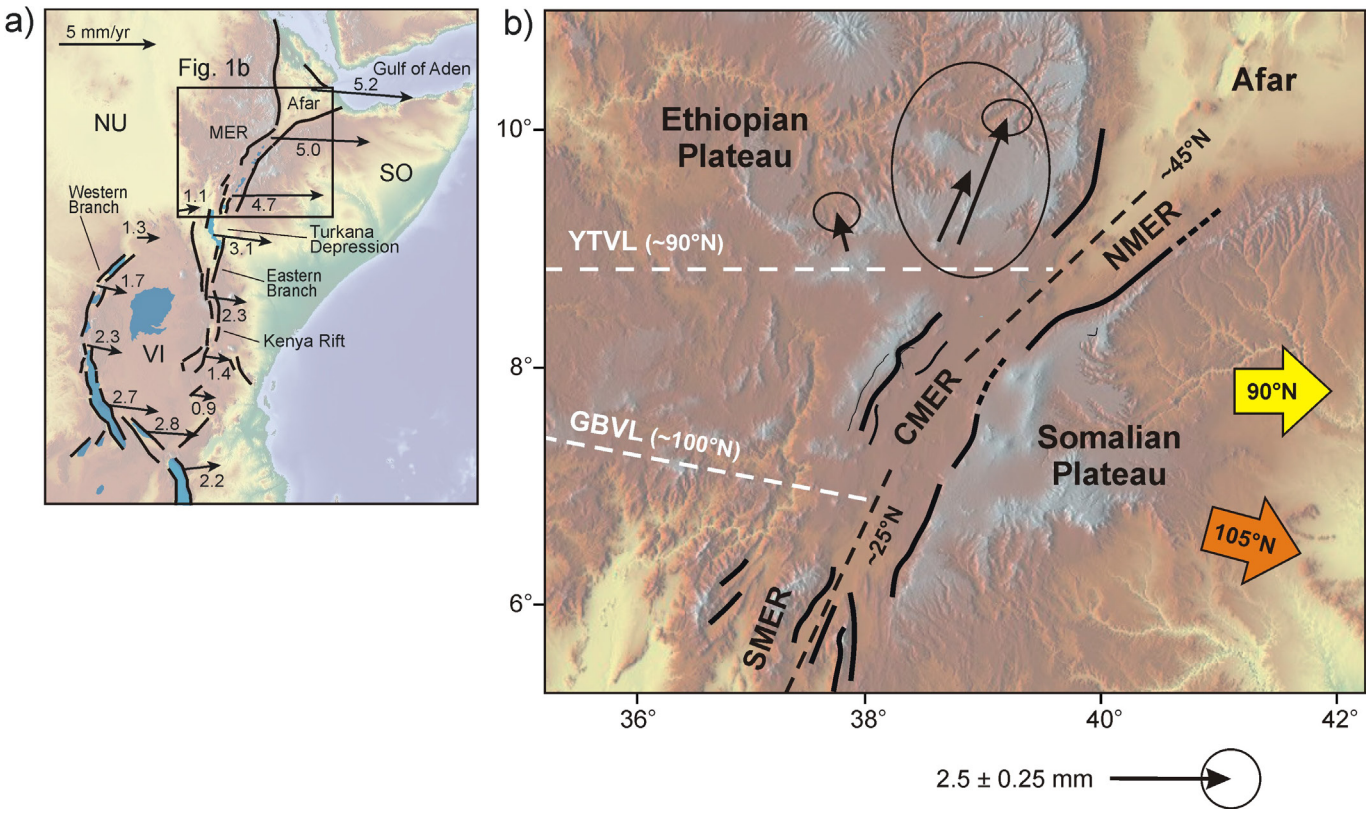

Figure 1 – **a)** Location of the Main Ethiopian Rift (MER) as the northern part of the East African Rift System, which splits the African continent in the Nubian Plate (NU) to the west and the Somalian Plate (SO) to the east (with the Victoria Microplate [VI] in between). GPS-based Somalian plate displacement with respect to ITRF08 (International Terrestrial Reference Frame 2008), after *Saria et al.* (2014). **b)** Distribution of the different sectors of the Main Ethiopian Rift and the associated volcano-tectonic lineaments. The yellow and orange arrows indicate the range of (long-term) plate divergence direction, i.e., E-W (90°N) and WNW-ESE (105°N), respectively (after *DeMets and Merkouriev*, 2016, 2021). Active displacement velocities along the YTVL is indicated with GPS velocities (incl. associated uncertainties) adopted from *Knappe et al.* (2020), who applied a Nubia-fixed frame using the ITRF2014-Nubia rotation vector. NMER: Northern MER, CMER: Central MER, SMER: Southern MER, YTVL: Yerer-Tullu Wellel Volcano-tectonic Lineament, GBVL: Goba-Bonga Volcano-tectonic lineament. Images Modified after *Keranen and Klemperer* (2008) and *Corti et al.* (2018a).

the trend of these faults varies from N-S in the south to 45°N in the north (e.g., *Agostini et al.*, 2011). In the southern and central MER, the boundary faults accommodate rifting with subordinate activity of the rift floor faults (*Corti et al.*, 2020). By contrast, in the northern MER, more than 50% of the rift opening is accommodated in ∼20 *km* wide, 60 *km* long magmatic segments (*Wolfenden et al.*, 2004). These along-axis variations in present-day deformation style have been interpreted to reflect different stages of rifting, where early stage-style rifting dominated by faulting occurs in the Southern MER, in contrast to late stage (break-up-style) rifting dominated by magmatism along the rift axis in the Northern MER (e.g., *Hayward and Ebinger*, 1996).

The transition between the different MER segments is defined by major structures (lineaments) oblique to the rift trend, extending hundreds of kilometres westward from the margins of the MER, on the Ethiopian Plateau (e.g., *Abebe Adhana*, 2014) (Figure 1b). The Yerer-Tullu Wellel Volcano-tectonic Lineament (YTVL *Abebe et al.*, 1998), which extends for some 700 *km* from the western margin of the MER to Tullu Wellel near the border with Sudan, is the most important of these oblique structures (Figure 1b). The YTVL separates the ca. 45°N striking Northern MER, where the undeformed crust of the plateau is ca. 50 *km* thick, from the Central MER, where the crust is ca. 40 *km* thick (Figure 1b *Keranen et al.*, 2009). The YTVL forms a tectono-magmatic system characterized by a roughly E-W alignment of E-W striking normal faults and major volcanic centres (e.g., *Abebe et al.*, 1998; *Tommasini et al.*, 2005; *Abebe Adhana*, 2014). Seismicity and geodetic data show that the YTVL is experiencing ongoing deformation, with higher rates of surface displacement in the east, i.e., near the MER, than in the west (*Keir et al.*, 2006, 2009; *Knappe et al.*, 2020). The second major oblique lineament is the Goba-Bonga Volcano-tectonic lineament (GBVL; e.g., *Merla et al.*, 1980; *Abbate and Sagri*, 1980; *Corti et al.*, 2018b), which marks the boundary between the Central MER and the Southern MER (Figure 1b). Here, the MER follows a ca. 25°N trend, compared to the ca. 45°N orientation of the Central and Northern MER (Figure 1b).

Both the YTVL and GBVL have likely been controlled by pre-existing Neoproterozoic weaknesses sub-parallel to the trend of the Gulf of Aden in the north, and oblique to the MER (e.g., *Abbate and Sagri*, 1980; *Abebe et al.*, 1998; *Korme et al.*, 2004; *Abebe Adhana*,

Table 1 – Model material properties

Granular materials	Quartz sand G12[a]	Corundum sand NKF120[b]
Grain size range (ϕ)	100-400 μm	90-120 μm
Specific density ($\rho_{specific}$)	2650 kg/m^3	4000 kg/m^3
Sieved density (ρ_{sieved})	1700 kg/m^3	2240 kg/m^3
Angle of internal peak friction (φ_{peak})	35°	37°
Coefficient of internal peak friction (μ_{peak})[c]	0.69	0.75
Angle of dynamic-stable friction (φ_{dyn})	29°	30°
Coefficient of dynamic-stable friction (μ_{dyn})[c]	0.55	0.57
Angle of reactivation friction (φ_{react})	32°	32°
Coefficient of reactivation friction (μ_{react})[c]	0.62	0.62
Cohesion (C)	50-110 Pa	100-150 Pa
Viscous materials	PDMS (G20OH)[d]	PDMS/corundum sand mixture[e]
Weight ratio PDMS : corundum sand	-	1:1
Density (ρ)	970 kg/m^3	ca. 1600 kg/m^3
Viscosity (η)	ca. $2 \cdot 10^4 Pa \cdot s^f$	ca. $1 \cdot 10^5 Pa \cdot s$
Rheology	Newtonian (n = ca. 1)[g]	near-Newtonian (n = 1.05-1.10)[g]

[a] Quartz sand properties after *Rosenau et al.* (2018)
[b] Corundum sand characteristics after *Rosenau and Pohlenz* (2023)
[c] $\mu = \tan(\varphi)$
[d] Pure PDMS (polydimethylsiloxane) rheology after *Rudolf et al.* (2016)
[e] PDMS-corundum mixture rheology after *Zwaan et al.* (2018a)
[f] Viscosity value holds for model strain rates ($< 10^{-4}/s$) (*Rudolf et al.*, 2016)
[g] Power-law exponent n (dimensionless) represents sensitivity to strain rate

2014; *Corti et al.*, 2018a, 2022). This interpretation is supported by geophysical data imaging a significant crustal thickness contrast along the YTVL (*Keranen and Klemperer*, 2008). Observed low P wave velocities at 75 km depth beneath the YTVL and GBVL (*Bastow et al.*, 2008) are explained by thermal anomalies and partial melting in response to upwelling and decompression of the asthenosphere; these processes contribute to further weakening of the lithosphere in correspondence to these oblique lineaments (e.g., *Corti et al.*, 2018a, 2022), as also supported by low values of the lithospheric elastic thickness (*Pérez-Gussinyé et al.*, 2009). It may be noted that the exact extent and width of these lineaments is not well defined in literature. Some authors present them as broader zones of tectonic (and volcanic) activity (e.g., *Corti et al.*, 2018b), whereas others see them as rather concentrated, linear features (e.g., *Keranen and Klemperer*, 2008), an interpretation we adopt in this modelling study.

Given that the orientation of these oblique lineaments is subparallel to the plate divergence, their activation and role in development of the MER remains to be clarified. *Keranen and Klemperer* (2008) suggested a two-phase rifting scenario, with an initial (Miocene) stage of rift development primarily controlled by lithospheric structures under a 130°N oriented plate divergence and a later (Pliocene-recent) phase of 105°N oriented plate divergence during which magmatic processes dominated. In the initial phase, rifting-related deformation would have been diverted away from the present-day MER, resulting in the activation of the YTVL; in the later phase, extensional deformation would have localized within the current rift valley to form the central MER. Modeling works (e.g., *Erbello et al.*, 2016; *Corti*, 2008) and plate kinematics analysis (e.g., *DeMets and Merkouriev*, 2016, 2021) argue against such a two-phase evolution, suggesting that MER rift kinematics have remained constant (under E-W [90°N] to ESE-WNW [105°N] plate divergence) since Miocene times. However, also if rift kinematics have remained constant, the ongoing deformation along the YTVL (*Keir et al.*, 2006, 2009; *Knappe et al.*, 2020) remains controversial, since its E-W orientation should be highly unfavourable for localizing deformation following various modelling studies (e.g., *Zwaan and Schreurs*, 2017; *Corti et al.*, 2018b; *Maestrelli et al.*, 2020; *Zou et al.*, 2024, see also Appendix B below). The same goes for any potential ongoing deformation along the GBVL.

Analogue tectonic modelling provides an excellent tool to study the dynamic evolution of rift systems, and many previous modelling studies analyzed the activation of structural weaknesses during single- and multiphase rifting (e.g., *Henza et al.*, 2010, 2011; *Zwaan et al.*, 2021, 2022; *Wang et al.*, 2021; *Maestrelli et al.*, 2020; *Zou et al.*, 2024). Nevertheless, despite these previous works, conclusive insights on how contemporaneous strain localization occurs along the structural lineaments in the MER, which are oriented sub-parallel to the divergence direction and thus unlikely to localize deformation, are still lacking. In this paper we apply analogue models that are specifically designed to replicate the situation in the MER to study how deformation may occur along the structural lineaments oblique to the MER, with a focus on the YTVL. Using these model results, we see how lineaments striking (near-)parallel to the plate divergence can in fact be activated during a single phase of rifting. As such, the multiphase deformation scenario proposed by *Keranen and Klemperer* (2008) is not required for the active deformation that is currently observed along the YTVL (and possibly GBVL). Instead, a simpler single-phase scenario that is more in line with plate tectonic reconstructions can be adopted.

2 Methods

2.1 Materials

In our models, we use both frictional and viscous materials to simulate brittle and ductile layers of the continental crust. A 3 *cm* thick layer of G12 quartz sand, which has a grain size range of 100-400 μm, an internal peak friction angle of 35°, a sieved density of 1700 kg/m^3, and a cohesion of 50-110 Pa (Table 1 *Rosenau et al.*, 2018), serves to represent a 22.5 *km* thick brittle upper crust. Below this sand layer, a 1 *cm* thick layer of viscous material simulates a 7.5 *km* thick ductile lower crust. This near-Newtonian viscous material is a mixture of G20OH polydimethylsiloxane (PDMS) and fine NKF120 Corundum sand, with a density of ca. 1600 kg/m^3 and a viscosity of $1{\cdot}10^5 Pa{\cdot}s$ (Table 1). Details on scaling are provided in Appendix A and Table A1 below.

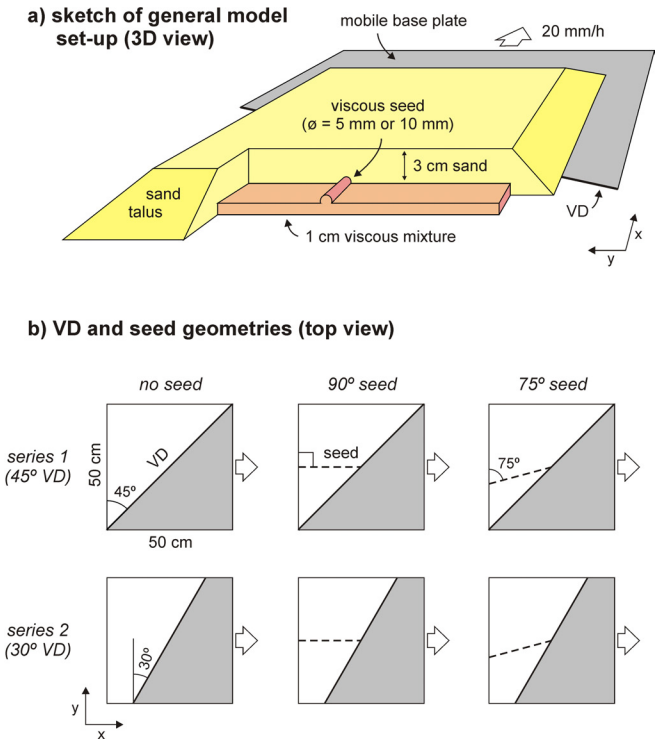

Figure 2 – Model set-up. (a) 3D sketch of model set-up and layering. (b) orientations of VD (velocity discontinuity) and seeds in the various models. The 45° oblique VD models of Series 1 represent an end-member situation with pure E-W (90°N) divergence in the MER, whereas the 30° oblique VD represent an end-member situation with ca. WNW-ESE (105°N) plate divergence in the MER. Seeds, representing crustal weaknesses in the models, are oriented either E-W (90°N) or ca. WSW-ENE (75°N). See also Table 2 for details on model parameters, and Appendix B below for a reference model R0 involving orthogonal divergence and a 90° seed.

2.2 General Model Set-up

Our model set-up, which is inspired by the one applied by *Zwaan et al.* (2021, 2022), involves a base plate placed below the two layers of model materials representing the upper and lower continental crust (Figure 2a). The base plate is pulled by precise computer-controlled stepper motors, moving it away from under the model materials so that the edge of the plate creates a velocity discontinuity (VD). This VD induced deformation in the overlying model materials, thus creating a rift structure along its length (e.g., *Tron and Brun*, 1991; *Bonini et al.*, 1997; *Keep and McClay*, 1997; *Michon and Merle*, 2000; *Zwaan et al.*, 2019; *Bonini et al.*, 2023), which can be considered analogous to the Main Ethiopian Rift in nature. Moreover, in order to simulate lineaments such as the YTVL and GBVL, we added "seeds", i.e., semi-circular ridges of viscous material on top of the viscous layer (Figure 2a). By doing so, we locally reduced the integrated strength of the sand layer, which leads to localization of deformation, apart from the deformation controlled by the VD (e.g., *Zwaan et al.*, 2021, 2022). In our models, this seed is intended to represent the linear character of inherited weakness linked to thermal anomalies and localized lithospheric thinning associated with pre-existing Neoproterozoic structures (*Abebe et al.*, 1998; *Korme et al.*, 2004; *Abbate and Sagri*, 1980; *Abebe Adhana*, 2014; *Corti et al.*, 2018a,b, Figure 1b). The 50 *cm* wide, 50 *cm* long and 4 *cm* high models were contained by sand taluses on each side, to prevent viscous materials from flowing out from below the overlying sand layer (Figure 2a).

Table 2 – Overview of model parameters

	Model name	VD (simulated MER) orientation*	Seed (simulated tectonic lineament) orientation	Seed diameter
-	R0**	0°	90°	10 *mm*
Series 1	R1	45°	-	-
	A1	45°	90°	5 *mm*
	A2	45°	90°	10 *mm*
	A3	45°	75°	5 *mm*
	A4	45°	75°	10 *mm*
Series 2	R2	30°	-	-
	B1	30°	90°	5 *mm*
	B2	30°	90°	10 *mm*
	B3	30°	75°	5 *mm*
	B4	30°	75°	10 *mm*

* VD: velocity discontinuity, MER: Main Ethiopian Rift. See Figures 1 and 2 for tectonic context and model set-up, respectively.

* Reference model presented in Appendix B below.

2.3 Model Parameters

In the main text we present a total of 10 models, split in two series, which are aimed to test the activation of lineaments in the context of the YTVL and MER (Figures 1, 2, Table 2). In the first series, we apply a 45° (measured in clockwise direction) oriented VD, which together with the 90° base plate motion direction would represent pure E-W (90°N) tectonic plate divergence end member in nature, given the ca 45°N orientation of the (Northern) MER (Figure 1). In the second series, we apply a 30° oriented VD, which in combination with the 90° base plate motion would represent a 105°N plate divergence direction end member in nature (Figure 3). Results of an additional reference model (R0) with a 0° VD orientation, serving to calibrate the model set-up with respect to previous analogue modelling works, is included in Appendix B below.

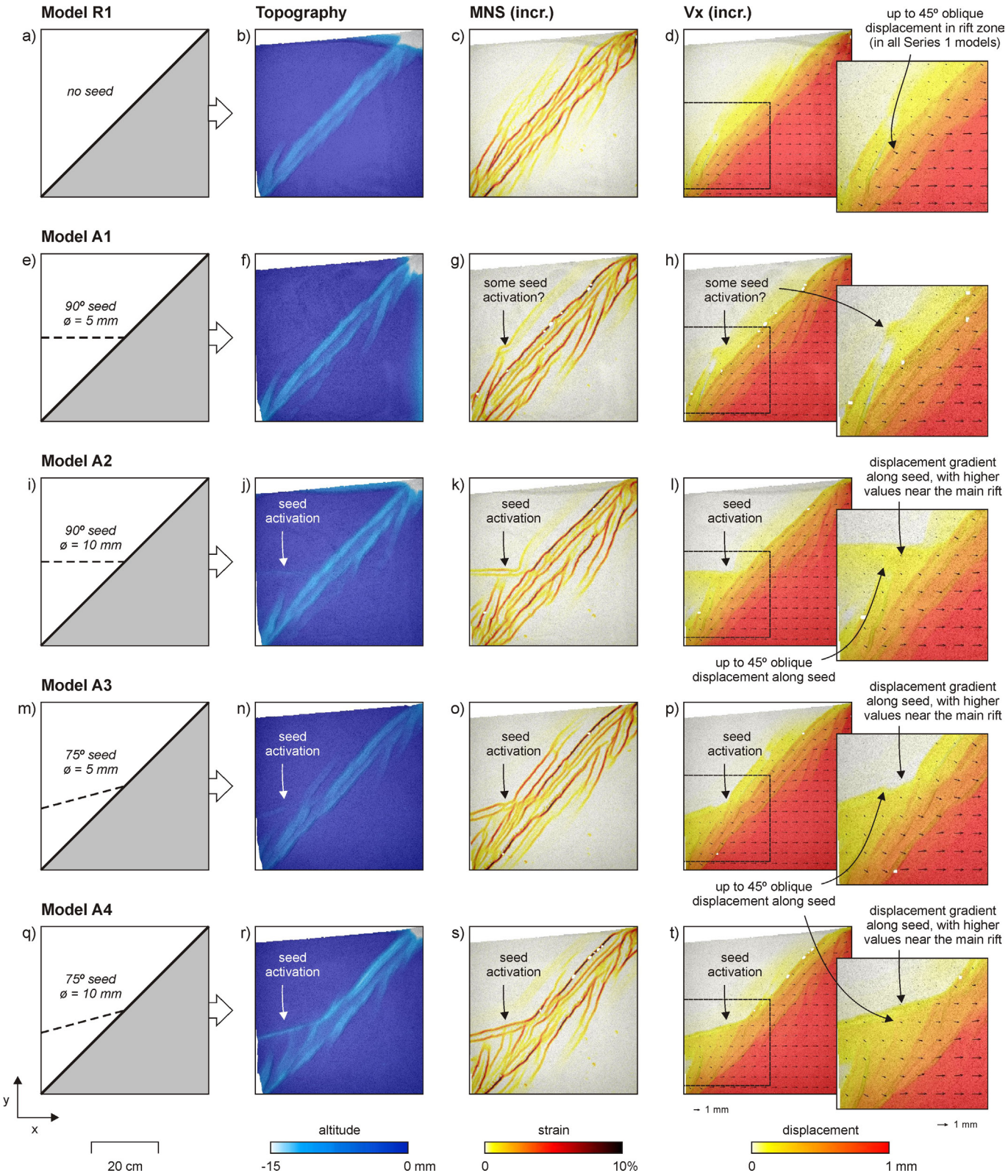

Figure 3 – Overview of model results from Series 1 at $t = 90$ *min* (base plate divergence = 30 *mm*), showing topography, incremental maximum normal strain (MNS, used as a proxy for active faulting), and displacement in the x-direction (i.e., the base plate motion direction). Vectors in the Vx maps indicate the full incremental displacement direction and magnitude. Incremental data are computed over 1 *mm* divergence (i.e. base plate displacement) intervals.

Moreover, both series contained a reference model without seed, as well as four models including seeds each. In these latter models, we vary the orientation of the seeds to explore the impact of pre-existing weakness orientation on lineament (re)activation. In addition, we vary the diameter of the seed (either 5 or 10 *mm*) to explore the impact of the structural inheritance's relative weakness on lineament (re)activation. In all models, the divergence velocity is 20 mm/h, translating to the 5 mm/yr as observed in the present-day MER (e.g., *Saria et al.*, 2014) (see Appendix A below for details

on scaling). The full model run duration is 90 *min*, amounting to a total of 30 *mm* of divergence.

Note that the base plate motion direction in our models follows the convention that the general eastward motion of the Somalian Plate is relative to a stable Nubian Plate, with the seeds placed in that part of the model that is underlain by an immobile base (Figures 1, 2). This asymmetric set-up could potentially generate different results to a set-up with the seeds placed on top of the mobile base plate. However, previous modelling studies with similar set-ups and weaknesses that are continuous on both sides of the VD generate highly similar structures (e.g., *Zwaan et al.*, 2021, 2022; *Bonini et al.*, 2023). As such, we should not expect the asymmetry of our set-up to affect the general model results in any significant manner.

2.4 Model Analysis

We use a digital image correlation technique (particle image velocimetry, PIV) for quantitative surface deformation monitoring (e.g., *Adam et al.*, 2005). A stereoscopic pair of two 12-bit, 29-megapixel monochrome cameras (LaVision Imager XLite 29M) is deployed to monitor surface deformation at high spatial (8 px/mm) and temporal resolution. One image is taken every 0.5 *mm* of displacement. Recorded image sequences are processed by commercial PIV software LaVision Davis 10.1 to derive the surface topography and the three-dimensional surface velocity (or incremental displacement) field, from which any component of the 3D surface incremental and cumulative strain tensor can be derived. To exclude boundary effects, we choose a central area of interest. The spatial resolution of the processed vector fields is 2 *mm* in terms of grid cell size and <5 μm in terms of displacement precision. For visualization and analysis of the surface deformation, we trace model topography and horizontal displacement over time. Moreover, we map the incremental horizontal maximum normal (or principal) strain as an absolute measure of strain.

3 Results

3.1 Series 1 Model Results

An overview of the results of the Series 1 models, all with a 45° VD orientation representing 90°N (E-W) plate divergence in nature (Figures 1, 2b), is provided in Figure 3. Reference model R1 shows the impact of the 45° oblique VD without the presence of a seed (Figure 3a-d). Deformation along the VD creates a ca. 6.5 *cm* wide graben that is bounded by both VD-parallel normal faults and a series of en echelon normal faults with a counterclockwise deviation in strike of ca. 20° with respect to the main graben trend. The displacement field shows how material above the mobile plate is displaced to the side, at the same rate as the plate. In the graben along the VD, this displacement is reduced, whereas minor displacement is registered on the graben shoulders on the opposite side. Velocities decrease stepwise across the graben structure, from general plate velocity in the model's "east" (above the mobile base plate) to zero in the model's "west" (above the stationary base). Steps in the velocity field correspond to faults. Moreover, the displacement field, which is parallel to the plate motion direction for the material above the mobile base plate has a different orientation in the rift zone itself, where horizontal displacement is ca. 45° oblique to the base plate motion direction (Figure 3d, inset). An overall very similar situation as in Model R1 occurs in Model A1, which has a 90° seed with a diameter of 5 *mm* that does not activate (Figure 3e-h).

By contrast, when increasing the diameter of the seed to 10 *mm* in Model A2, minor deformation is localized along the seed (Figure 3i-l). This localization of deformation is associated with additional displacement between the seed and the main graben, which both can be some 45° oblique with respect to the base plate motion direction (Figure 3l). Moreover, applying a 75° seed orientation in Model A3 allows a 5 *mm* diameter seed to be somewhat activated (Figure 3m-p), whereas a 10 *mm* seed in Model A4 causes significant localization of deformation (Fig. q-t), as best illustrated by the final model topography results (Figure 3r). In both cases, we observe additional displacement between seed and main graben, again up to some 45° oblique with respect to the base plate motion direction. However, it may be noted that in all models involving localization of deformation along the seeds, the structure of the main graben remains very similar (Figure 3i-t). Moreover, in all models that show the activation of a seed, we observe a gradual increase of horizontal displacement towards the main graben from west to east along the seed (insets in Figure 3l, p, t).

3.2 Series 2 Model Results

An overview of the results of our Series 2 models, all with a 30° VD orientation that represents 105°N (roughly WNW-ESE) plate divergence in nature (Figures 1, 2), are provided in Figure 4. Reference Model R2 illustrates the impact of the 30° oblique VD without a seed being present (Figure 4a-d). Similar to Model R1, we obtain a graben structure along the VD, including en echelon boundary faults striking ca. 15° counter-clockwise from the main graben. However, the graben itself is significantly wider in Model R2 than in Model R1 (7.5 *cm* vs. 6.5 *cm*, respectively). The displacement field also shows how material on top of the mobile plate is moving at the same rate as the plate, whereas this displacement is reduced in the graben, and minor displacement is recorded on the opposite graben shoulder (Figure 4d). The same result is obtained with Model B1, which contains a 5 *mm* thick seed that is oriented 90° and does not activate (similar to the equivalent seed in Model A1) (Figure 4e-h). As also observed in the Series 1 models, horizontal displacement within the rift zone in these Series 2 models is significantly oblique with respect to the base plate motion direction (Figure 3d,h,l,p,t and Figure 4d,h,l,p,t), albeit to a lower degree than in Series 1 (ca. 45° vs. 20°).

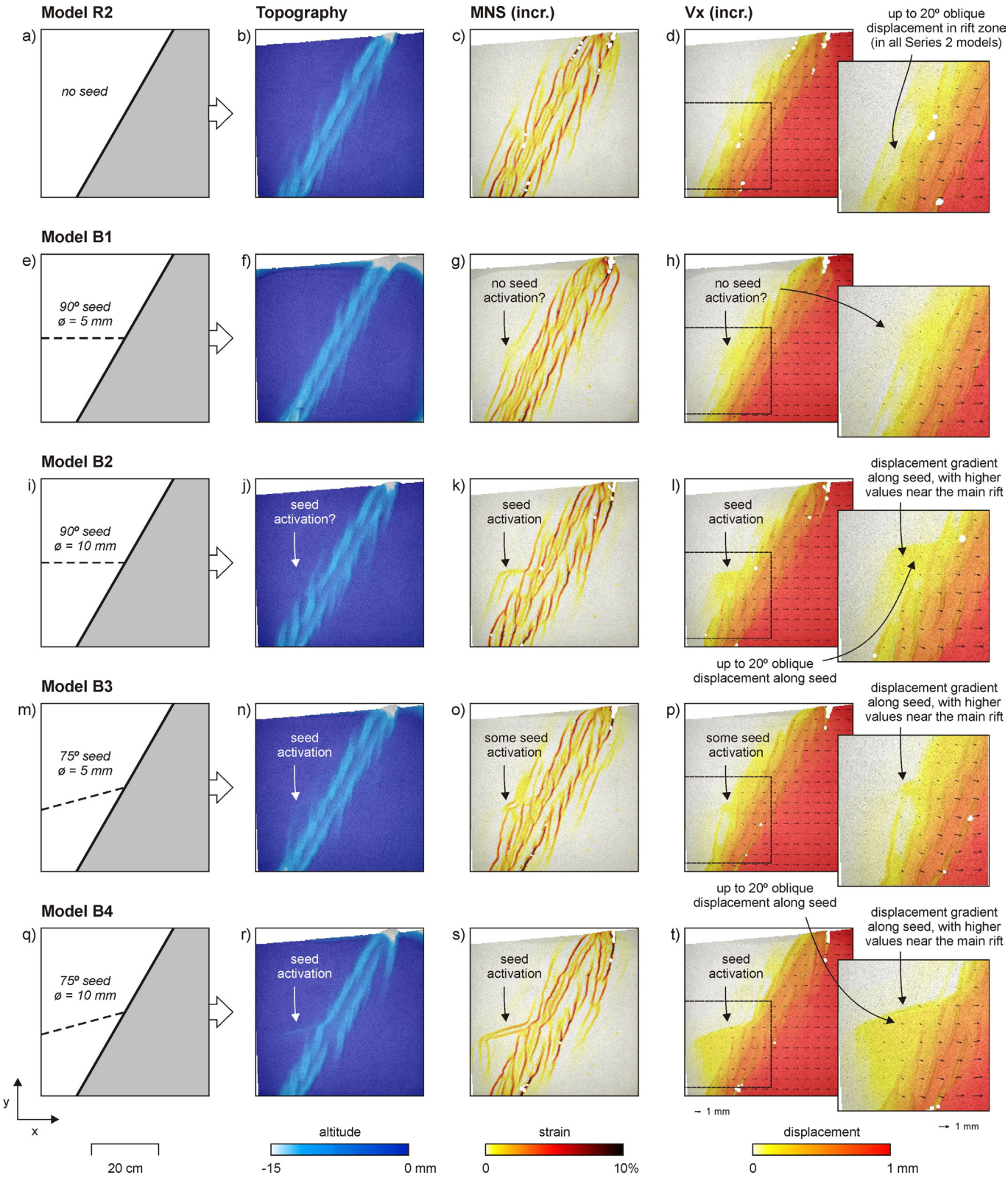

Figure 4 – Overview of model results from Series 2 at $t = 90$ *min* (base plate divergence = 30 *mm*), showing topography, incremental maximum normal strain (MNS, used as a proxy for active faulting), and displacement in the x-direction (i.e., the base plate motion direction). Vectors in the Vx maps indicate the full incremental displacement direction and magnitude. Incremental data are computed over 1 *mm* divergence (i.e. base plate displacement) intervals.

We do observe minor activation of the thicker (10 *mm*) seed in Model B2 (Figure 4i-l). When the 5 *mm* thick seed is oriented 75° in Model B3, we get slightly more localization of deformation (Figure 4m-p), but only when the seed diameter is increased to 10 *mm* in Model B4, we observe significant activation, similar to that in the Series 1 models (Figures 3, 4q-t). In the cases where the seed is activated, we observe increased displacement between the seed and main graben (with up to 20° obliquity with respect to the base plate motion direction), and a similar gradual increase of deformation closer to the main graben as in the Series 1 models (Figure 3l,p,t and Figure 4l,p,t).

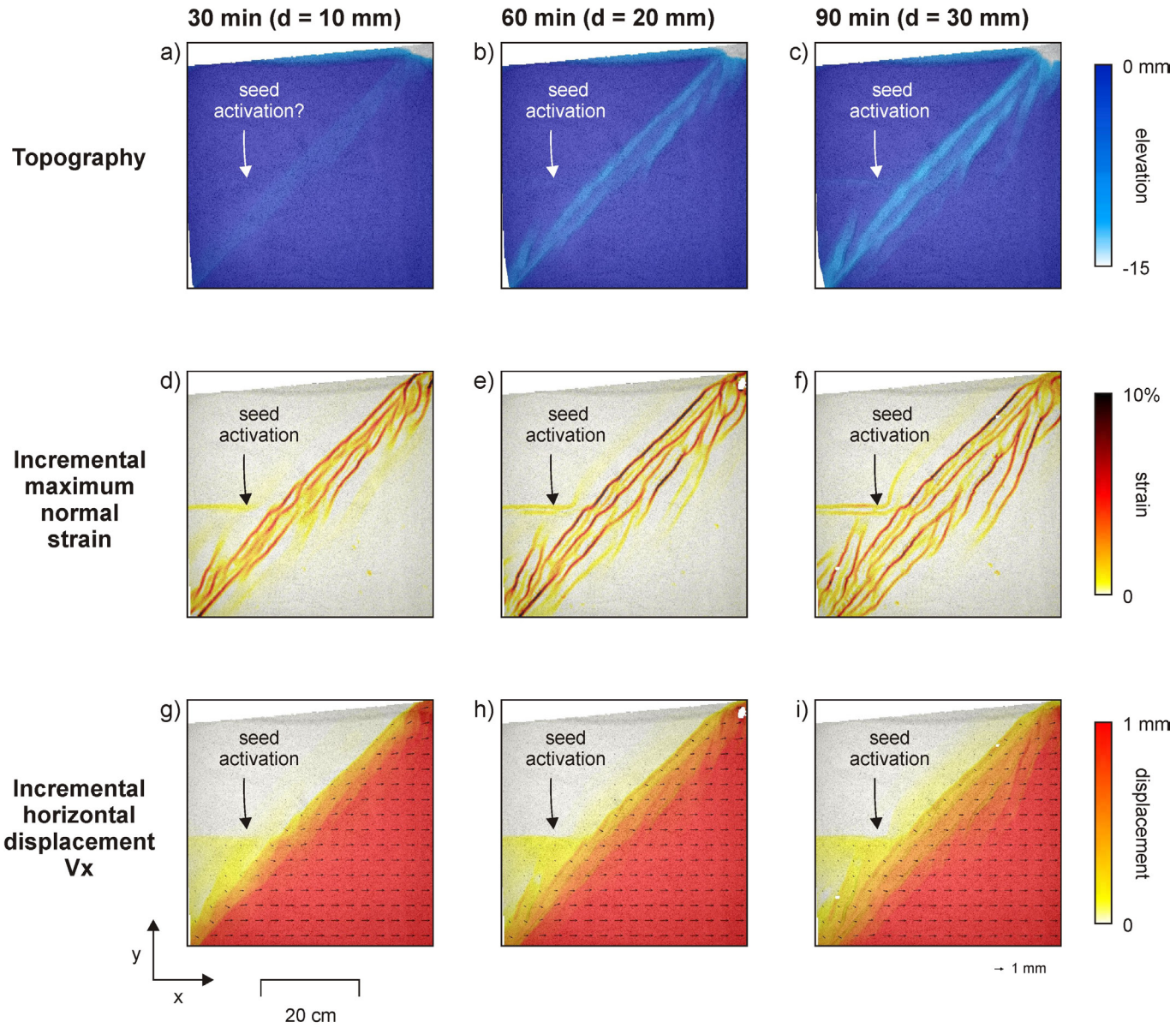

Figure 5 – Evolution of key Model A2 from Series 1 (45° VD and a 10 *mm* thick seed with a 90° orientation, representing the ca. E-W [90°N] plate divergence end-member in the Main Ethiopian Rift). Topography data are incremental, maximum normal strain and Vx-displacement data are incremental (computed over a 1 *mm* base plate divergence interval). Vectors in (g-i) indicate the full incremental displacement direction and magnitude. d = divergence (i.e., base plate displacement).

Yet it is clear that the impact of the seed on the surface structures in the Series 2 models is significantly reduced with respect to their equivalents in series 1 (Figures 3, 4). Finally, the main graben structure is very similar between all Series 2 models.

3.3 Detailed Analysis of Models A2 and B4

We provide a more detailed analysis of Models A2 and B4, which we consider key models since they may best represent the situation in the MER (see Section 4.2).

The evolution of Model A2, with a 45° VD orientation and a 90° striking seed of 10 *mm* diameter that would represent a 90°N (pure E-W) divergence setting in nature, is shown in Figure 5. We observe the gradual development of the main graben as it grows in both depth and width, as indicated by the topography evolution and the active fault patterns (Figure 5a-f). However, the active faulting and displacement data show how the seed localizes deformation from the earliest stages of the model run on (Figure 5d-i). Also the gradient towards the main graben is established early on (Figure 5g-i).

We show the evolution of Model B4, with a 30° VD orientation and a 75° striking seed of 10 *mm* diameter representing a 105°N (roughly WNW-ESE) divergence scenario in nature, in Figure 6. Similar to Model B4, the topography results and active faults show a gradual development of the main graben (Figure 6a-f), whereas the active faulting and displacement data show a similar activation of the seed since the early stages of the deformation (Figure 5d-i). Moreover, the gradient towards the main graben is established early on in Model B4 too (Figure 6g-i).

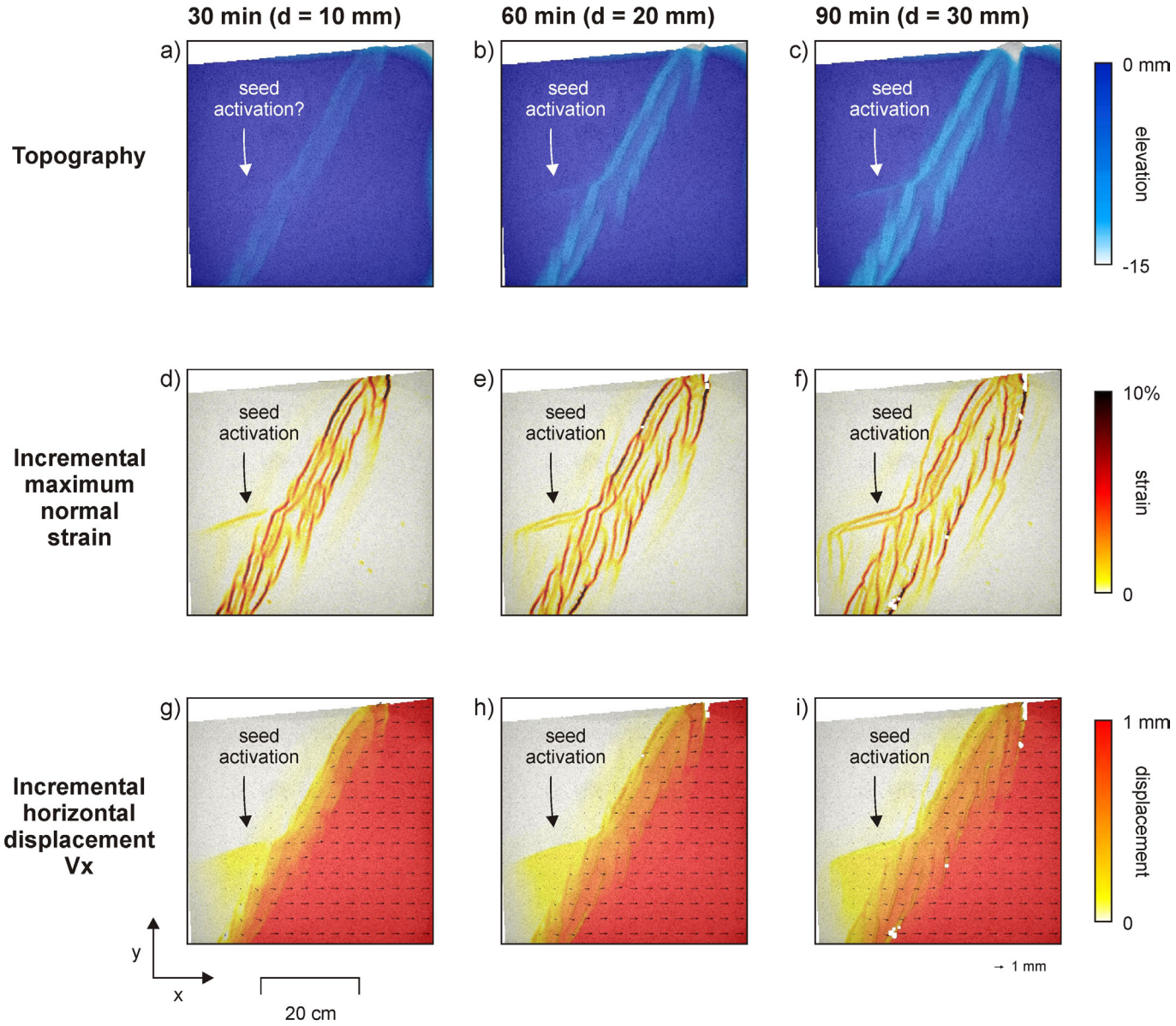

Figure 6 – Evolution of key Model B4 from Series 2 (30° VD orientation and a 10 *mm* thick seed with a 90° orientation, representing the ca. WNW-ESE [105°N] plate divergence end-member in the Main Ethiopian Rift). Topography data are incremental, maximum normal strain and Vx-displacement data are incremental (computed over a 1 *mm* base plate divergence interval). Vectors in (g-i) indicate the full incremental displacement direction and magnitude. d = divergence (i.e., base plate displacement).

4 Discussion

4.1 Interpretation of Model Results and Comparison with Previous Works

Our model set-up is tailored to the situation in the MER, but the results (as summarized in Figure 7) are very much in line with previously published modelling studies. The en echelon structures we observe in both reference models (R1 and R2) are characteristic of oblique rifting models (e.g., *Withjack and Jamison*, 1986; *Tron and Brun*, 1991; *Keep and McClay*, 1997; *Bonini et al.*, 1997; *Corti*, 2008; *Agostini et al.*, 2009; *Zwaan et al.*, 2022) (Figure 7a, b). Also the use of seeds as structural weaknesses has a clear precedent (e.g., *Le Calvez and Vendeville*, 2002; *Zwaan and Schreurs*, 2017; *Molnar et al.*, 2019, 2020; *Zwaan et al.*, 2021, 2022). The relative impact of such weaknesses, i.e., their activation as a function of the degree to which they locally reduce the strength of the brittle (sand) layer (in this study controlled by the diameter of the seed, Figure 7c, d) fits with observations from previous works as well (*Osagiede et al.*, 2021; *Zwaan et al.*, 2021; *Bonini et al.*, 2023). Moreover, we find that the orientation of the (crustal) weakness is of great importance for its activation (Figure 7e, f); weaknesses that are oriented near-orthogonal to the divergence direction tend to activate much better than those oriented oblique to the divergence direction, as also observed in *Zwaan et al.* (2021, 2022); *Bonini et al.* (2023); *Zou et al.* (2024). Even so, we do observe the activation of seeds that are (near-)parallel to the divergence direction in our models with oblique rifts (Figure 7c-h), which is in contrast to previous modelling works where such activation of crustal weaknesses does

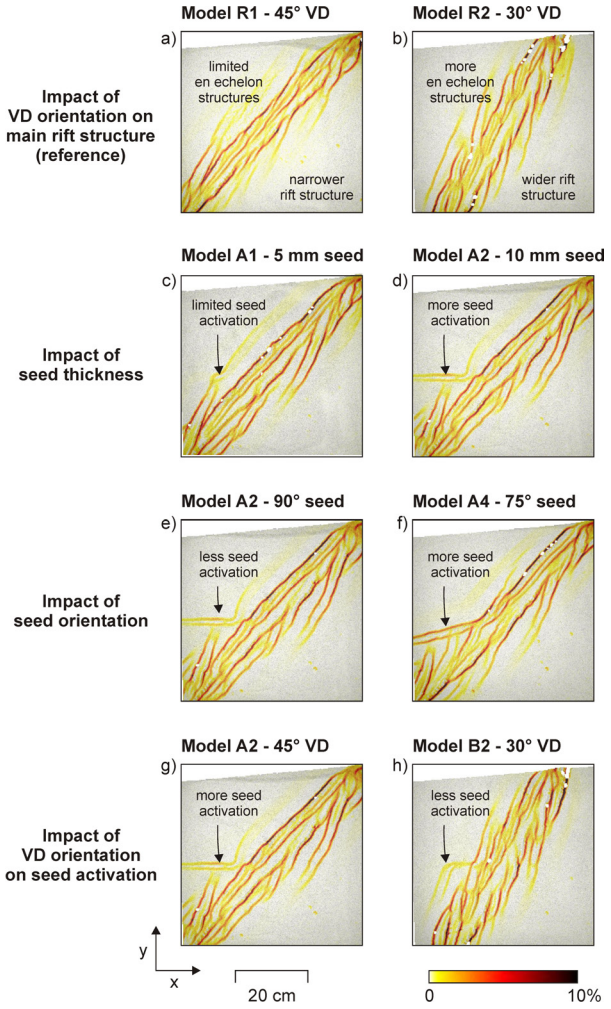

Figure 7 – Summary figure highlighting the impact of the various parameters tested on tectonic lineament activation. The top view incremental maximum normal strain (MNS) images depict the situation at the end of the model run (i.e., after 90 *min*, or 30 *mm* of divergence).

not occur at all (e.g., *Zwaan and Schreurs*, 2017; *Corti et al.*, 2018b; *Zou et al.*, 2024).

The key to this conundrum is the obliquity of the main rift structure, a factor not really explored in previous works, which focussed on the orientation of the seeds (or pre-cut faults) instead. We interpret that the oblique rift arrangement in our present study induces local reorientation of extensional strain that allow for activation of these otherwise unfavourably oriented seeds (Figure 8). We base this interpretation on the strain reorientation analysis pioneered by *Withjack and Jamison* (1986) (see also *Fournier and Petit*, 2007, for more details): oblique rifts cause local reorientation of the regional extensional strain direction that follows the plate divergence direction. Instead, the local maximum extensional strain orientation (ε_{h1}) is the bisection of the regional plate divergence direction and the normal to the rift (Figure 8c). This relation between plate divergence and local strain direction explains the oblique orientation of the en echelon faulting that is typical of oblique rifting (e.g., *Withjack and Jamison*, 1986; *Tron and Brun*, 1991; *Keep and McClay*, 1997; *Bonini et al.*, 1997; *Agostini et al.*, 2009; *Corti et al.*, 2013; *Zwaan et al.*, 2022, Figures 3-8).

In a first step, we propose that the reoriented local extensional strain could be sufficiently oblique with respect to the seed to allow for deformation to localize, given that the horizontal displacements along the seeds in the models (45° and 20° oblique to the base plate motion directions for a 45° and 30° oblique VD, respectively, see insets in Figures 3, 4) are more or less in line with the theoretical local maximum extensional strain orientation (a 22.5° oblique extensional strain direction for a 45° VD, see the example in 8c-f, or 15° oblique for a 30° VD). Furthermore, in a second step we can speculate that the presence of the seed itself may even cause a second reorientation of the local extensional strain within the rift deformation zone ($\varepsilon_{h1(2)}$), since the seed itself is oblique to the local strain direction there, further promoting localization of deformation along the seed (Figure 8g). Such a second strain reorientation brings us closer to the 45° oblique horizontal displacement (with respect to the base plate motion direction) as observed in the 45° VD models (Figures 3, 8g). Moreover, the strain reorientation effect of the oblique rift should be expected to wane the farther away from the rift one looks, which is what we see in our models, where displacement and strain values along the seed are smaller farther away from the main rift structure.

Our local strain reorientation interpretation is further supported by the impact of the specific VD orientation observed in our models. In the 30° VD (Series 2) models we find that the seeds localize less deformation than in the 45° (Series 1) models (Figure 7g, h). This is due to the VD in the Series 1 models being less well oriented for localizing normal faulting than in the Series 2 models (the ideal VD orientation being 0° for orthogonal rifting, Figure 8a, b), allowing for a more oblique local extensional strain direction and thus more opportunity for the seed to attract (part of the) deformation instead. A somewhat similar interplay between seeds and VDs with different (but minor) obliquities is also observed by *Zwaan et al.* (2021, 2022), where a more oblique VD allowed for a clearly enhanced development of deformation along seeds.

Before moving to an application of our model results to interpret the situation in the MER, we should point out a couple of limitations to our crustal scale modelling approach. We do not include magmatism and diking that is widespread in the MER and known to localize deformation along the rift axis, nor do we apply surface processes or lithospheric-scale isostasy. The exclusion of magmatism is however permissible, since we are focussing on the development of the YTVL, which is a lineament outside of the magma-rich MER. Moreover, the YTVL is characterized by a limited, mostly inactive volcanism (*Abebe et al.*, 1998); therefore, the contribution of magmatic processes to its development and evolution is negligible. The omission of both surface processes and isostasy is reasonable due to the limited impact these processes are expected to have on the large-scale structural arrangement and general

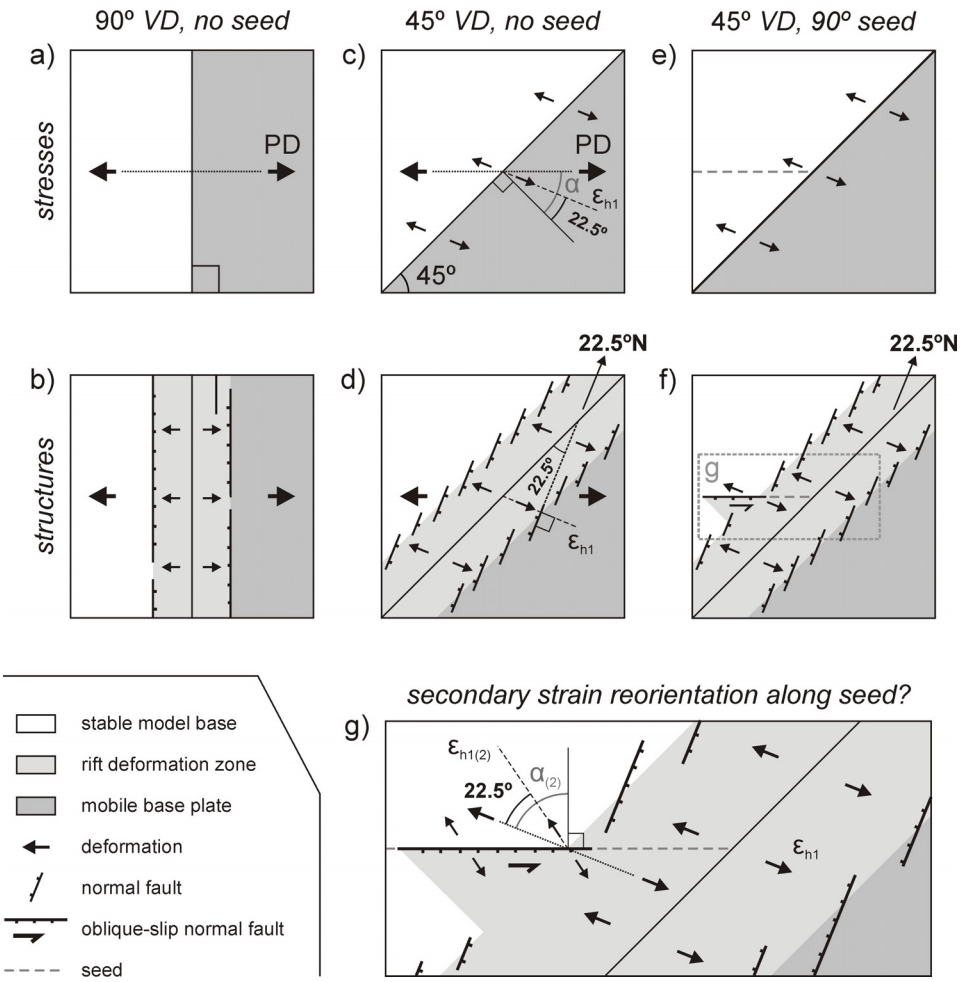

Figure 8 – Interpretation of local extensional strain reorientation and lineament activation enabled by an (45°) oblique rift, based on theory pioneered by *Withjack and Jamison* (1986) (see also *Fournier and Petit*, 2007). **(a-b)** A rift orthogonal to the plate divergence direction (PD) is ideal for through-going normal fault as they form perpendicular to the direction of maximum extensional strain, which is equal to the plate divergence direction in this case. Under such conditions, a seed oriented (near-)parallel to the plate divergence direction would not localize deformation (see also *Zwaan and Schreurs*, 2017; *Corti et al.*, 2018b; *Maestrelli et al.*, 2020; *Bonini et al.*, 2023; *Zou et al.*, 2024, and Appendix B below). **(c-d)** An oblique rift, without a seed, causes local extensional strain reoriented leading to en echelon normal faulting, with individual faults striking perpendicular to the local maximum extensional strain direction (ε_{h1}). **(e-f)** A seed oriented (near-)parallel to the divergence direction can activate due to the local strain reorientation caused by an oblique rift. **(g)** Potential secondary extensional strain reorientation ($\varepsilon_{h1(2)}$) of the initial local rift-induced extensional strain orientation (ε_{h1}) due to the obliquity of the seed with respect to the latter, further enhancing the likelihood of seed activation. Compare the orientation of the strain vectors with the horizontal displacement patterns in Figures 3-6.

tectonic evolution of early-stage rift systems such as the MER (*Zwaan et al.*, 2018b). Therefore, despite these limitations, our modelling work captures the main tectonic characteristics of the MER and its main oblique lineament.

4.2 Interpretation of Model Results with Respect to the Natural Example

Several scenarios have been proposed to explain the development of the MER and the YTVL. *Keranen and Klemperer* (2008) propose that deformation along the YTVL ceased since $\sim 2\ Ma$ (Pliocene-recent), due to a shift in plate kinematics. However, this polyphase tectonic model has been questioned by several modelling and field observations that suggest that the current plate motion along the MER has been constant since at least the mid-Miocene (e.g., *Erbello et al.*, 2016; *DeMets and Merkouriev*, 2021), while a constant opening direction of the MER best explains the basinward localization of deformation over the past 2 Myr (*Corti*, 2008; *Muluneh et al.*, 2020). Even so, insights from previous tectonic modelling studies (e.g., *Zwaan and Schreurs*, 2017; *Corti et al.*, 2018b; *Zwaan et al.*, 2021, 2022; *Bonini et al.*, 2023) suggest that unfavourably oriented structures, such as the YTVL, should not have been active under such roughly E-W plate divergence. As such, the simultaneous deformation along the MER and YTVL has remained an enigma.

Our novel analogue modelling study now enables us to propose a solution to this enigma. When comparing our new model results to the situation in the MER, we find that both Model A2 and Model B4 (when rotated 15° clockwise) reproduce the first-order observations in nature (Figure 9). In both models, the MER develops

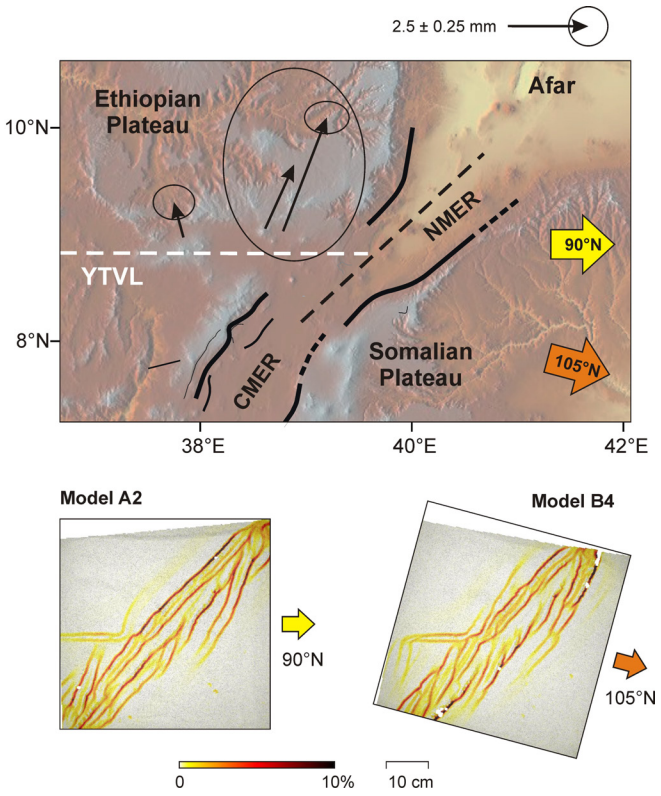

Figure 9 – Comparison between model results and natural situation in the central and northern Main Ethiopian Rift. The model A2 and B4 maximum normal strain (indicating active faulting) results at $t = 90$ *min* (30 *mm* or displacement) show a good fit, indicating that both 90°N and 105°N plate motion end members (adopted from DeMets and Merkouriev 2016; 2021) can allow for activation of the Yerer-Tullu Wellel Volcano-tectonic Lineament (YTVL). NMER: Northern MER, CMER: Central MER. Image modified after *Keranen and Klemperer* (2008); *Corti et al.* (2018a). Active displacement along the YTVL (incl. associated uncertainties) is indicated with GPS velocities adopted from *Knappe et al.* (2020), who used a Nubia-fixed frame using the ITRF2014-Nubia rotation vector.

while the YTVL is activated as an extensional lineament, likely due to local extensional strain changes linked to the interaction between the oblique MER and YTVL (see section 4.1 and Figure 8). Moreover, we observed an increase in deformation activity towards the modelled MER, as is also the case in nature (*Keir et al.*, 2006; *Knappe et al.*, 2020, Figure 9). The simultaneous development of the MER and YTVL during a single continuous rifting phase, because of their particular orientation, is thus shown to have been possible without the need for the multiphase scenario put forward by *Keranen and Klemperer* (2008).

Moreover, as the GBVL has a somewhat similar orientation with respect to the MER as does the YTVL (Figure 1b), the tectonic arrangement could also have allowed for its activation during single-phase MER rifting. Future GPS analysis and tectonic fieldwork may confirm this hypothesis.

5 Conclusion

We have conducted a series of analogue tectonic models that are specifically designed to replicate the situation in the Main Ethiopian Rift (MER), in order to study how deformation may localize along the structural lineaments associated to the rift, despite their highly unfavourable orientation with respect to the regional divergence direction. Our model results lead us to the following conclusions:

- Surprisingly, the activation of lineaments along weaknesses that are oriented (near-)parallel to the plate divergence direction is indeed possible, if (1) the weakness sufficiently reduced the strength of the crust to allow for deformation localization, and (2) the main rift trend is sufficiently oblique to the plate divergence direction, likely allowing for a local reorientation of extensional strain leading to lineament activation, even if this lineament is otherwise highly unfavourably oriented.
- The multiphase deformation scenario for the MER- and Yerer-Tullu Wellel Volcano-tectonic Lineament (YTVL) evolution as proposed by *Keranen and Klemperer* (2008) is not required for development of the YTVL. Instead, our models show that a single-phase scenario, which is more in line with plate tectonic reconstructions, can be adopted.
- Similarly, we may expect active deformation along the Goba-Bonga Volcano-tectonic lineament (GBVL), which has a similar orientation as the YTVL, and a similar arrangement with respect to the MER.

The insights from our study, especially the observation that single-phase rifting can activate unfavourably aligned lineaments, may be of use beyond the MER as well, since many rift systems around the world involve weaknesses and lineaments that have activated, as well as various degrees of oblique divergence (e.g., *Brune et al.*, 2018). Examples may be the various basins along the East African Rift System, the Red Sea and South Atlantic (see e.g., *Molnar et al.*, 2019, 2020).

Acknowledgements

We thank Frank Neumann and Thomas Ziegenhagen for technical assistance in the lab, Uwe Lemgo for IT support, and Kirsten Elger for helping us prepare a GFZ data publication containing the supplementary material (*Zwaan et al.*, 2025). Frank Zwaan received financial support in the form of a GFZ Discovery Fellowship and an Equality Grant from the Faculty of Geosciences and Environment at the University of Lausanne. Ameha Muluneh has been funded by German Research Foundation (DFG, 537025018), Jun Liu received financial support from the China Scholarship Council (CSC NO. 202006190038). Giacomo Corti acknowledges the support of the European Plate Observing System (EPOS) and the Joint Research Unit (JRU) EPOS Italia. We kindly thank reviewers Laetitia le Pourhiet and Anindita Samsu for their valuable

feedback, as well as TEKTONIKA editors Janine Kavanagh and Guillaume Duclaux for handling the manuscript, and Mohamed Gouiza for the copy-editing and typesetting.

Author contributions

Conceptualization: FZ, AM, MR, JL, EK
Methodology: FZ, AM, MR, JL, EK
Formal analysis: FZ, AM, MR, JL, EK
Investigation: all authors
Validation: all authors
Visualization: FZ, MR, JL, EK
Resources: MR
Data Curation: FZ, MR, JL, EK
Writing - Original draft: all authors
Writing - Review & Editing: all authors
Project administration: FZ

Data availability

A GFZ data publication (Zwaan et al. 2025) containing an overview of the models completed for this study is publicly accessible via this link: https://doi.org/10.5880/fidgeo.2025.041.

Competing interests

The authors declare no competing interests.

Peer review

This publication was peer-reviewed by Laëtitia Le Pourhiet and Anindita Samsu. The full peer-review report can be found here: Review Report.

Copyright notice

References

Abbate, E., and M. Sagri (1980), Volcanites of Ethiopian and Somali Plateaus and major tectonic lines, *Atti Convegni Lincei*, *47*, 219–227.

Abebe, T., F. Mazzarini, F. Innocenti, and P. Manetti (1998), The Yerer-Tullu Wellel volcanotectonic lineament: a transtensional structure in central Ethiopia and the associated magmatic activity, *Journal of African earth sciences (Oxford, England: 1994)*, *26*(1), 135–150, https://doi.org/10.1016/s0899-5362(97)00141-3.

Abebe Adhana, T. (2014), The occurrence of a complete continental rift type of volcanic rocks suite along the Yerer–Tullu Wellel Volcano Tectonic Lineament, Central Ethiopia, *Journal of African earth sciences (Oxford, England: 1994)*, *99*, 374–385, https://doi.org/10.1016/j.jafrearsci.2014.02.008.

Adam, J., J. L. Urai, B. Wieneke, O. Oncken, K. Pfeiffer, N. Kukowski, J. Lohrmann, S. Hoth, W. van der Zee, and J. Schmatz (2005), Shear localisation and strain distribution during tectonic faulting—new insights from granular-flow experiments and high-resolution optical image correlation techniques, *Journal of structural geology*, *27*(2), 283–301, https://doi.org/10.1016/j.jsg.2004.08.008.

Agostini, A., G. Corti, A. Zeoli, and G. Mulugeta (2009), Evolution, pattern, and partitioning of deformation during oblique continental rifting: Inferences from lithospheric-scale centrifuge models: CENTRIFUGE MODELS OF OBLIQUE RIFTING, *Geochemistry, geophysics, geosystems: G(3)*, *10*(11), https://doi.org/10.1029/2009gc002676.

Agostini, A., M. Bonini, G. Corti, F. Sani, and F. Mazzarini (2011), Fault architecture in the Main Ethiopian Rift and comparison with experimental models: Implications for rift evolution and Nubia–Somalia kinematics, *Earth and planetary science letters*, *301*(3-4), 479–492, https://doi.org/10.1016/j.epsl.2010.11.024.

Bastow, I. D., A. A. Nyblade, G. W. Stuart, T. O. Rooney, and M. H. Benoit (2008), Upper mantle seismic structure beneath the Ethiopian hot spot: Rifting at the edge of the African low-velocity anomaly: ETHIOPIAN UPPER MANTLE SEISMIC STRUCTURE, *Geochemistry, geophysics, geosystems: G(3)*, *9*(12), https://doi.org/10.1029/2008gc002107.

Bonini, L., U. Fracassi, N. Bertone, F. E. Maesano, G. Valensise, and R. Basili (2023), How do inherited dip-slip faults affect the development of new extensional faults? Insights from wet clay analog models, *Journal of structural geology*, *169*(104836), 104,836, https://doi.org/10.1016/j.jsg.2023.104836.

Bonini, M., T. Souriot, M. Boccaletti, and J. P. Brun (1997), Successive orthogonal and oblique extension episodes in a rift zone: Laboratory experiments with application to the Ethiopian Rift, *Tectonics*, *16*(2), 347–362, https://doi.org/10.1029/96TC03935.

Brune, S., S. E. Williams, and R. D. Müller (2018), Oblique rifting: the rule, not the exception, *Solid earth*, *9*(5), 1187–1206, https://doi.org/10.5194/se-9-1187-2018.

Buck, W. R. (1991), Modes of continental lithospheric extension, *Journal of geophysical research*, *96*(B12), 20,161–20,178, https://doi.org/10.1029/91JB01485.

Byerlee, J. (1978), Friction of rocks, *Pure and applied geophysics*, *116*(4-5), 615–626, https://doi.org/10.1007/bf00876528.

Corti, G. (2008), Control of rift obliquity on the evolution and segmentation of the main Ethiopian rift, *Nature geoscience*, *1*(4), 258–262, https://doi.org/10.1038/ngeo160.

Corti, G. (2009), Continental rift evolution: From rift initiation to incipient break-up in the Main Ethiopian Rift, East Africa, *Earth-science reviews*, *96*(1-2), 1–53, https://doi.org/10.1016/j.earscirev.2009.06.005.

Corti, G., M. Philippon, F. Sani, D. Keir, and T. Kidane (2013), Re-orientation of the extension direction and pure

extensional faulting at oblique rift margins: comparison between the Main Ethiopian Rift and laboratory experiments, *Terra nova*, *25*(5), 396–404, https://doi.org/10.1111/ter.12049.

Corti, G., P. Molin, A. Sembroni, I. D. Bastow, and D. Keir (2018a), Control of pre-rift lithospheric structure on the architecture and evolution of continental rifts: Insights from the main Ethiopian rift, east Africa, *Tectonics*, *37*(2), 477–496, https://doi.org/10.1002/2017tc004799.

Corti, G., F. Sani, S. Agostini, M. Philippon, D. Sokoutis, and E. Willingshofer (2018b), Off-axis volcano-tectonic activity during continental rifting: Insights from the transversal Goba-Bonga lineament, Main Ethiopian Rift (East Africa), *Tectonophysics*, *728-729*, 75–91, https://doi.org/10.1016/j.tecto.2018.02.011.

Corti, G., F. Sani, A. A. Florio, T. Greenfield, D. Keir, A. Erbello, A. A. Muluneh, and A. Ayele (2020), Tectonics of the Asela-langano margin, main Ethiopian rift (east Africa), *Tectonics*, *39*(8), e2020TC006,075, https://doi.org/10.1029/2020tc006075.

Corti, G., D. Maestrelli, and F. Sani (2022), Large-to local-scale control of pre-existing structures on continental rifting: Examples from the Main Ethiopian Rift, East Africa, *Frontiers in earth science*, *10*, https://doi.org/10.3389/feart.2022.808503.

DeMets, C., and S. Merkouriev (2016), High-resolution estimates of Nubia–Somalia plate motion since 20 Ma from reconstructions of the Southwest Indian Ridge, Red Sea and Gulf of Aden, *Geophysical journal international*, *207*(1), 317–332, https://doi.org/10.1093/gji/ggw276.

DeMets, C., and S. Merkouriev (2021), Detailed reconstructions of India-Somalia plate motion, 60 Ma to present: Implications for Somalia plate absolute motion and India-Eurasia plate motion, *Geophysical journal international*, *227*(3), 1730–1767, https://doi.org/10.1093/gji/ggab295.

Erbello, A., G. Corti, A. Agostini, F. Sani, T. Kidane, and A. Buccianti (2016), Modeling along-axis variations in fault architecture in the Main Ethiopian Rift: Implications for Nubia-Somalia kinematics, *Journal of geodynamics*, *102*, 24–38, https://doi.org/10.1016/j.jog.2016.07.002.

Fournier, M., and C. Petit (2007), Oblique rifting at oceanic ridges: Relationship between spreading and stretching directions from earthquake focal mechanisms, *Journal of structural geology*, *29*(2), 201–208, https://doi.org/10.1016/j.jsg.2006.07.017.

Hayward, N. J., and C. J. Ebinger (1996), Variations in the along-axis segmentation of the Afar Rift system, *Tectonics*, *15*(2), 244–257, https://doi.org/10.1029/95TC02292.

Henza, A. A., M. O. Withjack, and R. W. Schlische (2010), Normal-fault development during two phases of non-coaxial extension: An experimental study, *Journal of structural geology*, *32*(11), 1656–1667, https://doi.org/10.1016/j.jsg.2009.07.007.

Henza, A. A., M. O. Withjack, and R. W. Schlische (2011), How do the properties of a pre-existing normal-fault population influence fault development during a subsequent phase of extension?, *Journal of structural geology*, *33*(9), 1312–1324, https://doi.org/10.1016/j.jsg.2011.06.010.

Hubbert, M. K. (1937), Theory of scale models as applied to the study of geologic structures, *Geological Society of America bulletin*, *48*(10), 1459–1520, https://doi.org/10.1130/GSAB-48-1459.

Keep, M., and K. R. McClay (1997), Analogue modelling of multiphase rift systems, *Tectonophysics*, *273*(3-4), 239–270, https://doi.org/10.1016/s0040-1951(96)00272-7.

Keir, D., C. J. Ebinger, G. W. Stuart, E. Daly, and A. Ayele (2006), Strain accommodation by magmatism and faulting as rifting proceeds to breakup: Seismicity of the northern Ethiopian rift, *Journal of geophysical research*, *111*(B5), https://doi.org/10.1029/2005JB003748.

Keir, D., I. J. Hamling, A. Ayele, E. Calais, C. Ebinger, T. J. Wright, E. Jacques, K. Mohamed, J. O. S. Hammond, M. Belachew, E. Baker, J. V. Rowland, E. Lewi, and L. Bennati (2009), Evidence for focused magmatic accretion at segment centers from lateral dike injections captured beneath the Red Sea rift in Afar, *Geology*, *37*(1), 59–62, https://doi.org/10.1130/G25147A.1.

Keranen, K., and S. L. Klemperer (2008), Discontinuous and diachronous evolution of the Main Ethiopian Rift: Implications for development of continental rifts, *Earth and planetary science letters*, *265*(1-2), 96–111, https://doi.org/10.1016/j.epsl.2007.09.038.

Keranen, K. M., S. L. Klemperer, J. Julia, J. F. Lawrence, and A. A. Nyblade (2009), Low lower crustal velocity across Ethiopia: Is the Main Ethiopian Rift a narrow rift in a hot craton?, *Geochemistry, geophysics, geosystems: G(3)*, *10*(5), https://doi.org/10.1029/2008GC002293.

Knappe, E., R. Bendick, C. Ebinger, Y. Birhanu, E. Lewi, M. Floyd, R. King, G. Kianji, N. Mariita, T. Temtime, B. Waktola, B. Deresse, M. Musila, J. Kanoti, and M. Perry (2020), Accommodation of east African rifting across the Turkana depression, *Journal of geophysical research. Solid earth*, *125*(2), e2019JB018,469, https://doi.org/10.1029/2019jb018469.

Korme, T., V. Acocella, and B. Abebe (2004), The role of pre-existing structures in the origin, propagation and architecture of faults in the main Ethiopian rift, *Gondwana research: international geoscience journal*, *7*(2), 467–479, https://doi.org/10.1016/s1342-937x(05)70798-x.

Le Calvez, J. H., and B. C. Vendeville (2002), Experimental designs to model along-strike fault interaction, *Journal of the virtual explorer*, *07*, 1441–8142, https://doi.org/10.3809/jvirtex.2002.00043.

Maestrelli, D., D. Montanari, G. Corti, C. Del Ventisette, G. Moratti, and M. Bonini (2020), Exploring the interactions between rift propagation and inherited crustal fabrics through experimental modeling, *Tectonics*, *39*(12), e2020TC006,211, https://doi.org/10.1029/2020tc006211.

Merla, G., E. Abbate, A. Azzaroil, P. Bruni, P. Canuti, M. Fazzuoli, M. Sagri, and P. Tacconi (1980), A geological map of Ethiopia and Somalia at 1/2.000.000, and comment with a map of major landforms, *Earth-science reviews*, *16*, 388, https://doi.org/10.1016/0012-8252(80)90110-5.

Michon, L., and O. Merle (2000), Crustal structures of the Rhinegraben and the Massif Central grabens: An experimental approach, *Tectonics*, *19*(5), 896–904, https://doi.org/10.1029/2000TC900015.

Michon, L., V. Famin, and X. Quidelleur (2022), Evolution of the East African Rift System from trap-scale to plate-scale rifting, *Earth-science reviews*, *231*(104089), 104,089, https://doi.org/10.1016/j.earscirev.2022.104089.

Molnar, N., A. Cruden, and P. Betts (2020), The role of inherited crustal and lithospheric architecture during the evolution of the Red Sea: Insights from three dimensional analogue experiments, *Earth and planetary science letters*, *544*(116377), 116,377, https://doi.org/10.1016/j.epsl.2020.116377.

Molnar, N. E., A. R. Cruden, and P. G. Betts (2019), Interactions between propagating rifts and linear weaknesses in the lower crust, *Geosphere*, *15*(5), 1617–1640, https://doi.org/10.1130/ges02119.1.

Mulugeta, G. (1988), Squeeze box in a centrifuge, *Tectonophysics*, *148*(3-4), 323–335, https://doi.org/10.1016/0040-1951(88)90139-4.

Muluneh, A. A., S. Brune, F. Illsley-Kemp, G. Corti, D. Keir, A. Glerum, T. Kidane, and J. Mori (2020), Mechanism for deep crustal seismicity: Insight from modeling of deformation processes at the Main Ethiopian Rift, *Geochemistry, geophysics, geosystems: G(3)*, *21*(7), e2020GC008,935, https://doi.org/10.1029/2020gc008935.

Osagiede, E. E., M. Rosenau, A. Rotevatn, R. Gawthorpe, C. A.-L. Jackson, and M. Rudolf (2021), Influence of zones of pre-existing crustal weakness on strain localization and partitioning during rifting: Insights from analog modeling using high-resolution 3D digital image correlation, *Tectonics*, *40*(10), e2021TC006,970, https://doi.org/10.1029/2021tc006970.

Pérez-Gussinyé, M., M. Metois, M. Fernández, J. Vergés, J. Fullea, and A. R. Lowry (2009), Effective elastic thickness of Africa and its relationship to other proxies for lithospheric structure and surface tectonics, *Earth and planetary science letters*, *287*(1-2), 152–167, https://doi.org/10.1016/j.epsl.2009.08.004.

Ramberg, H. (1981), *Gravity, deformation and the earth's crust: In theory, experiments and geological application*, 2 ed., Academic Press, San Diego, CA.

Rosenau, M., and A. Pohlenz (2023), Ring-shear test data of corundum sand "NKF120" used for analogue modelling in the experimental tectonics laboratory at GFZ Potsdam, https://doi.org/10.5880/GFZ.4.1.2023.009.

Rosenau, M., A. Pohlenz, H. Kemnitz, and M. Warsitzka (2018), Ring-shear test data of quartz sand G12 used for analogue experiments in the Helmholtz Laboratory for Tectonic Modelling (HelTec) at the GFZ German Research Centre for Geosciences in Potsdam, https://doi.org/10.5880/GFZ.4.1.2019.003.

Rudolf, M., D. Boutelier, M. Rosenau, G. Schreurs, and O. Oncken (2016), Rheological benchmark of silicone oils used for analog modeling of short- and long-term lithospheric deformation, *Tectonophysics*, *684*, 12–22, https://doi.org/10.1016/j.tecto.2015.11.028.

Saria, E., E. Calais, D. S. Stamps, D. Delvaux, and C. J. H. Hartnady (2014), Present-day kinematics of the east African rift, *Journal of geophysical research. Solid earth*, *119*(4), 3584–3600, https://doi.org/10.1002/2013jb010901.

Schellart, W. P. (2000), Shear test results for cohesion and friction coefficients for different granular materials: scaling implications for their usage in analogue modelling, *Tectonophysics*, *324*(1-2), 1–16, https://doi.org/10.1016/s0040-1951(00)00111-6.

Stamps, D. S., C. Kreemer, R. Fernandes, T. A. Rajaonarison, and G. Rambolamanana (2021), Redefining East African Rift System kinematics, *Geology*, *49*(2), 150–155, https://doi.org/10.1130/g47985.1.

Tommasini, S., P. Manetti, F. Innocenti, T. Abebe, M. Sintoni, and S. Conticelli (2005), The Ethiopian subcontinental mantle domains: geochemical evidence from Cenozoic mafic lavas, *Mineralogy and petrology*, *84*(3-4), 259–281, https://doi.org/10.1007/s00710-005-0081-9.

Tron, V., and J.-P. Brun (1991), Experiments on oblique rifting in brittle-ductile systems, *Tectonophysics*, *188*(1-2), 71–84, https://doi.org/10.1016/0040-1951(91)90315-j.

Wang, L., D. Maestrelli, G. Corti, Y. Zou, and C. Shen (2021), Normal fault reactivation during multiphase extension: Analogue models and application to the Turkana depression, East Africa, *Tectonophysics*, *811*(228870), 228,870, https://doi.org/10.1016/j.tecto.2021.228870.

Weijermars, R., and H. Schmeling (1986), Scaling of Newtonian and non-Newtonian fluid dynamics without inertia for quantitative modelling of rock flow due to gravity (including the concept of rheological similarity), *Physics of the earth and planetary interiors*, *43*(4), 316–330, https://doi.org/10.1016/0031-9201(86)90021-x.

Withjack, M. O., and W. R. Jamison (1986), Deformation produced by oblique rifting, *Tectonophysics*, *126*(2-4), 99–124, https://doi.org/10.1016/0040-1951(86)90222-2.

Wolfenden, E., C. Ebinger, G. Yirgu, A. Deino, and D. Ayalew (2004), Evolution of the northern Main Ethiopian rift: birth of a triple junction, *Earth and planetary science letters*, *224*(1-2), 213–228, https://doi.org/10.1016/j.epsl.2004.04.022.

Zou, Y., D. Maestrelli, G. Corti, C. Del Ventisette, L. Wang, and C. Shen (2024), Influence of inherited brittle fabrics on continental rifting: Insights from centrifuge experimental modeling and application to the East African Rift System, *Tectonics*, *43*(1), e2023TC007,947, https://doi.org/10.1029/2023tc007947.

Zwaan, F., and G. Schreurs (2017), How oblique extension and structural inheritance influence rift segment interaction: Insights from 4D analog models, *Interpretation*, *5*(1), SD119–SD138, https://doi.org/10.1190/int-2016-0063.1.

Zwaan, F., and G. Schreurs (2020), Rift segment interaction in orthogonal and rotational extension experiments: Implications for the large-scale development of rift systems, *Journal of structural geology*, *140*(104119), 104,119, https:

//doi.org/10.1016/j.jsg.2020.104119.

Zwaan, F., and G. Schreurs (2023), The link between Somalian Plate rotation and the East African Rift System: an analogue modelling study, *Solid earth*, *14*(8), 823–845, https://doi.org/10.5194/se-14-823-2023.

Zwaan, F., G. Schreurs, M. Ritter, T. Santimano, and M. Rosenau (2018a), Rheology of PDMS-corundum sand mixtures from the Tectonic Modelling Lab of the University of Bern (CH), https://doi.org/10.5880/FIDGEO.2018.023.

Zwaan, F., G. Schreurs, and J. Adam (2018b), Effects of sedimentation on rift segment evolution and rift interaction in orthogonal and oblique extensional settings: Insights from analogue models analysed with 4D X-ray computed tomography and digital volume correlation techniques, *Global and planetary change*, *171*, 110–133, https://doi.org/10.1016/j.gloplacha.2017.11.002.

Zwaan, F., G. Schreurs, and S. J. H. Buiter (2019), A systematic comparison of experimental set-ups for modelling extensional tectonics, *Solid earth*, *10*(4), 1063–1097, https://doi.org/10.5194/se-10-1063-2019.

Zwaan, F., P. Chenin, D. Erratt, G. Manatschal, and G. Schreurs (2021), Complex rift patterns, a result of interacting crustal and mantle weaknesses, or multiphase rifting? Insights from analogue models, *Solid earth*, *12*(7), 1473–1495, https://doi.org/10.5194/se-12-1473-2021.

Zwaan, F., P. Chenin, D. Erratt, G. Manatschal, and G. Schreurs (2022), Competition between 3D structural inheritance and kinematics during rifting: Insights from analogue models, *Basin research*, *34*(2), 824–854, https://doi.org/10.1111/bre.12642.

Zwaan, F., A. A. Muluneh, J. Liu, E. Kosari, M. Rosenau, G. Corti, and F. Sani (2025), Results of analogue tectonic models of rifting and tectonic lineament reactivation along the Main Ethiopian Rift, https://doi.org/10.5880/fidgeo.2025.041.

Appendix A: Model Scaling

Model scaling procedures serve to ensure that the model adequately represents the situation in nature. Since brittle materials have time-independent rheology, the main scaling concern is the internal friction angle of the quartz sand in our models (35°), which is falls well in the ranges of values observed in natural upper crustal rocks (31–38°; *Byerlee*, 1978, Table A1). Yet when scaling viscous materials representing the ductile lower crust, one needs to take into account their strain rate-dependent rheology. We start with the basis equation describing the stress ratio between model and nature σ^*:

$$\sigma^* = \rho^* \cdot h^* \cdot g^* \tag{1}$$

where ρ^* is the density ratio, h^* the length ratio, and g^* the gravity ratio between model an nature (*Hubbert*, 1937). We can subsequently compute the strain rate $\dot{\varepsilon}^*$ from the stress ratio σ^* and viscosity ratio η^*:

$$\dot{\varepsilon} = \frac{\sigma^*}{\eta^*} \tag{2}$$

When assuming a relatively high lower crustal viscosity of $5 \cdot 10^{21}\ Pa \cdot s$ in nature, which may be representative of the situation in early-stage rift systems (e.g., *Buck*, 1991), $1\ h$ in our models translates to ca. $3\ Myr$ in nature. Consequently, the model divergence velocity we apply represents a plate divergence velocity of ca. $5\ mm/yr$ in nature, which is very close to the values in the MER (e.g., *Saria et al.*, 2014).

Moreover, we can assess the dynamic similarity between our models and nature by comparing the R_s number and the Ramberg number R_m. The R_s number represents the ratio between gravitational stress and cohesion C in the brittle model materials and the upper crustal layers they represent (*Mulugeta*, 1988; *Ramberg*, 1981):

$$R_s = \frac{gravitational\ stress}{cohesive\ strength} = \frac{\rho \cdot g \cdot h}{C} \tag{3}$$

The cohesion of 50 Pa in our sand, combined with an assumed cohesion of 50 MPa in natural rocks (e.g., *Schellart*, 2000, and references therein) yields an R_s value of 10 in both model and nature.

The Ramberg number is relevant to the dynamic similarity of the viscous model materials with respect to their ductile equivalents in nature, and assesses the ratio between gravitational stress and viscous strength (*Weijermars and Schmeling*, 1986):

$$R_m = \frac{gravitational\ stress}{viscous\ strength} = \frac{\rho \cdot g \cdot h^2}{\eta \cdot v} \tag{4}$$

Following our calculations, the R_m number is 1.9 in both models and nature. Given that both the R_s and R_m model values are similar to those for the natural equivalent, we can consider our models properly scaled for the simulation of early-stage rifting, such as in the MER. All relevant scaling parameters used in this study are provided in Table A1.

Table A1 – Scaling parameters

		Model	Nature
General parameters	Gravitational acceleration (g)	$9.81\ m/s^2$	$9.81\ m/s^2$
	Extension velocity (v)	$5.6 \cdot 10^{-5}\ m/s$	$1.6 \cdot 10^{-10}\ m/s$
Brittle layer	Material	Quartz sand	Upper crust
	Peak internal friction angle (ϕ_{peak})	35°	30-38°
	Thickness (h)	$3 \cdot 10^{-2}\ m$	$2.25 \cdot 10^{4}\ m$
	Density (ρ)	$1700\ kg/m^3$	$2800\ kg/m^3$
	Cohesion (C)	$50\ Pa$	$6.0 \cdot 10^{7}\ Pa$
Viscous/ductile layer	Material	PDMS/corundum sand mix	Lower crust
	Thickness (h)	$1 \cdot 10^{-2}\ m$	$7.5 \cdot 10^{4}\ m$
	Density (ρ)	$1600\ kg/m^3$	$2900\ kg/m^3$
	Viscosity (η)	$1.5 \cdot 10^{5}\ Pa \cdot s$	$5 \cdot 10^{21} Pa \cdot s$
Dynamic scaling values	Brittle stress ratio (R_s)	10	10
	Ramberg number (R_m)	1.9	1.9

Appendix B: Reference model R0

Next to the models presented in the main text, we present an additional reference model R0, which is intended to verify the non-activation of divergence-parallel seeds as observed in previous modelling studies with similar general set-ups (e.g., *Zwaan and Schreurs*, 2017; *Corti*, 2008; *Maestrelli et al.*, 2020; *Bonini et al.*, 2023; *Zou et al.*, 2024) (Figure B1). In this set-up, which involves a 10 *mm* thick seed, which enhances the likelihood of deformation localizing, no deformation is observed along the seed. We thus confirm that our model results are in line with those from previous studies, and that an oblique rift and associated local extensional strain reorientation is required to allow activation of (near-)divergence-parallel weaknesses.

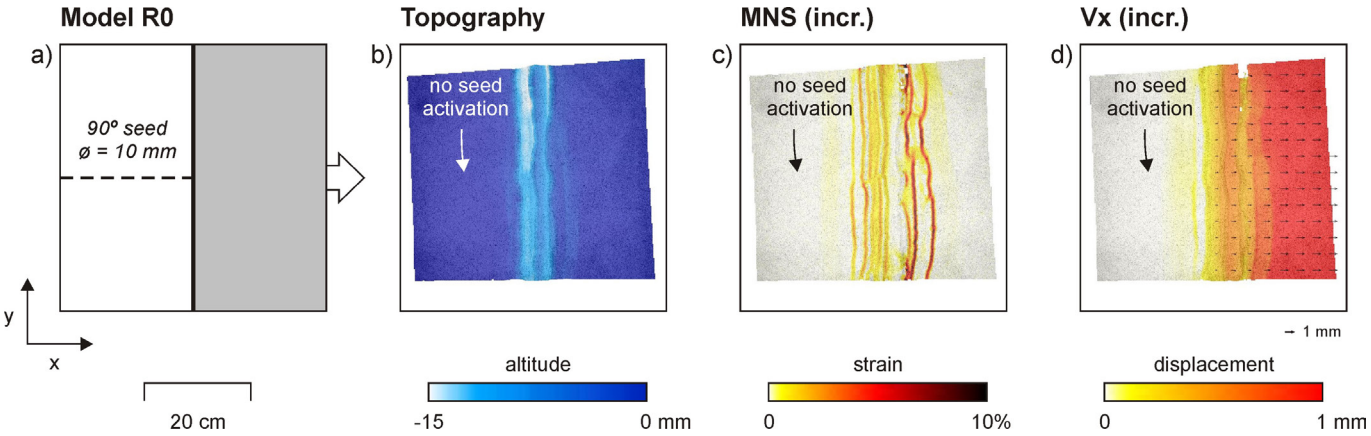

Figure B1 – Overview of model results from Model R0 at $t = 90\,min$ (base plate divergence = 30 *mm*), showing topography, incremental maximum normal strain (MNS, used as a proxy for active faulting), and displacement in the x-direction (i.e., the base plate motion direction). Vectors in the Vx maps indicate the full incremental displacement direction and magnitude. Incremental data are computed over a 1 *mm* base plate divergence interval.